

Monitoring fine-scale vegetation cover change using UAV-mounted multispectral cameras: A practical approach

Justin James van Blerk (✉ jvanblerk@gmail.com)

University of Cape Town <https://orcid.org/0000-0003-1626-3270>

Adam West

University of Cape Town

Julian Smit

University of Cape Town

Res Altwegg

University of Cape Town

Michael Timm Hoffman

University of Cape Town

Research Article

Keywords: UAV, pseudoinvariant features, NDVI, vegetation, area cover, multispectral, radiometric normalisation, remote sensing; post-fire; shrublands

Posted Date: February 22nd, 2022

DOI: <https://doi.org/10.21203/rs.3.rs-1337718/v1>

License:  This work is licensed under a Creative Commons Attribution 4.0 International License.

[Read Full License](#)

1 **Monitoring fine-scale vegetation cover change using UAV-mounted multispectral cameras: A practical**
2 **approach**

3 J. J. van Blerk ^a (Author for correspondence, jvanblerk@gmail.com, +27 83 271 4215),

4 A. G. West ^a, J. Smit ^b, R. Altwegg ^c, M. T. Hoffman ^d

5

6 ^aDepartment of Biological Sciences, University of Cape Town, Private Bag X3, Rondebosch 7701, South Africa

7 ^bDepartment of Geomatics, University of Cape Town, Private Bad X3, Rondebosch 7701, South Africa

8 ^cCentre for Statistics in Ecology, Environment and Conservation, Department of Statistical Sciences, University
9 of Cape Town, Private Bag X3, Rondebosch 7701, South Africa

10 ^dPlant Conservation Unit, Department of Biological Sciences, University of Cape Town, Private Bag X3,
11 Rondebosch 7701, South Africa

12

13 ORCID ID's:

14 J.J.vanBlerk: 0000-0003-1626-3270

15 A.G.West: 0000-0002-9352-9282

16 M.T.Hoffman: 0000-0002-5843-2397

17 R.Atwegg: 0000-0002-4083-6561

18 J.Smit: 0000-0001-8664-8059

19

20

21

22

23 **Abstract:**

- 24 1. Monitoring fine-scale vegetation processes over wider spatial extents is often logistically challenging.
- 25 2. We demonstrate a practical approach for monitoring high-resolution (i.e sub-meter) vegetation cover
- 26 change using UAV-mounted multispectral cameras. We use the post-fire shrublands of the Cape
- 27 Floristic Region, South Africa as a case study.
- 28 3. Repeated NDVI images of post-fire sites were generated biannually over three years using UAV-
- 29 mounted multispectral cameras and commercial, image-processing software. We applied a procedure
- 30 for identifying and correcting temporal radiometric noise in repeated NDVI images using
- 31 pseudoinvariant features (PIFs). We then extracted vegetation cover data using NDVI thresholding.
- 32 The quality of UAV-based vegetation cover data was assessed using detailed ground-truthing.
- 33 4. Relative radiometric image normalization reduced radiometric noise in NDVI data and resulted in
- 34 stronger correlations between UAV-based and ground-based area cover measurements over time.
- 35 5. UAV-mounted multispectral cameras are effective high-resolution vegetation monitoring tools which
- 36 could help ecologists to investigate fine-scale vegetation processes across wider spatial extents.

37

38

39

40

41 **Keywords:** UAV, pseudoinvariant features, NDVI, vegetation, area cover, multispectral, radiometric

42 normalisation, remote sensing; post-fire; shrublands

43

44

45

46

47 **1. Introduction:**

48 Monitoring changes in vegetation cover is central to understanding dynamic ecosystems. Changes in vegetation
49 cover could relate to a variety of important vegetation processes including post-disturbance recovery
50 ([Veraverbeke et al., 2012](#); [Gitas et al., 2013](#)), succession, ecosystem degradation or land use change
51 ([Cammeraat et al., 2005](#)), growth seasonality ([Shoshany et al., 1995](#)) or responses to climate change ([Port et
52 al., 2012](#)). The recent introduction of affordable unmanned aerial vehicles (UAVs) and lightweight multispectral
53 cameras has promised to deliver unprecedented accuracy of land cover change, yet there remain significant
54 challenges to overcome as ecologists adopt this technology ([Rasmussen et al., 2016](#)).

55 Typically, studies monitoring vegetation change have suffered a trade-off between scale and resolution. For
56 example, fine-scale physiological or demographic studies ([West et al., 2012](#); [Esler et al., 2015](#); [van Blerk et
57 al., 2021 a,b](#)) are often carried out over a relatively small area or conducted using a small sample of target
58 species. The detailed, high-effort nature of such measurements can provide a mechanistic understanding of
59 vegetation processes but also limits the spatial coverage which is logistically possible in the study. On the other
60 end of the scale, regional or landscape-level patterns in vegetation are generally investigated through aerial or
61 satellite imagery ([Cramer & Hoffman, 2015](#); [Slingsby et al., 2020](#)). While this type of imagery makes it
62 possible to study broad patterns over vast regions of the Earth's surface, the information generated from these
63 studies is only as detailed as the resolution and detail of the available imagery. Generally, satellite imagery is
64 too coarse to detect individual plant responses ([Aplin, 2005](#)), thus limiting the effectiveness of this data in
65 studies which require the detection of very fine-scale vegetation processes. Notwithstanding, vegetation studies
66 have attempted to bridge the gap between fine-scale and broad-scale resolution by employing methods of
67 estimation for assessing vegetation at intermediate scales. This includes using measures such as 'area cover' or
68 'canopy density'. Unfortunately, many of these methods of assessing vegetation at intermediate scales can be
69 problematic. For example, visual estimates of area cover tend to be subjective and are difficult to keep
70 consistent over a study period ([Bergstedt et al., 2009](#)).

71 UAVs offer the possibility of monitoring fine-scale vegetation processes over larger spatial scales, essentially
72 bridging the gap between fine-scale and regional level studies. Many important vegetation processes (e.g. shrub
73 resprouting after fire) occur at the sub meter resolution and thus require finer resolution monitoring tools for
74 their detection. This technology is currently being applied to high precision agriculture ([Zhang & Kovacs,
75 2012](#); [Duveiller & Defourny, 2010](#); [Marcial-Pablo et al. 2019](#)) and is becoming more commonly used in a

76 wide range of ecological studies (e.g. [van Iersel et al., 2018](#); [Estrany et al. 2019](#); [Sotille et al., 2020](#); [Slingsby](#)
77 [et al., 2020](#)). Quantifying vegetation cover change using repeated imagery can be effective using vegetation
78 indices which are representative of some ecological or biophysical process ([Aplin, 2005](#)). The normalized
79 difference vegetation index (NDVI) ([Tucker, 1979](#)) is perhaps the most commonly used vegetation index in
80 remote sensing, providing an indication of photosynthetic activity. NDVI makes use of the high absorption of
81 red light in leaf material and a high reflectance of near infrared (NIR) light to differentiate plants from non-
82 photosynthetic materials within an image. This phenomenon can be useful for accurately computing high
83 resolution vegetation area cover from NDVI images ([Ghazal et al., 2015](#); [Marcial-Pablo et al. 2019](#)).

84 Tracking high-resolution environmental patterns in time-series data is challenging if measurement-related
85 inconsistencies occur within the time-series ([Bao et al., 2012](#); [Zhou et al., 2016](#)). This can result from human
86 subjectivity in measurement, or calibration issues related to measurement instruments. Such measurement-
87 induced noise should be identified and normalised before any meaningful environmental patterns can be
88 extracted from the data. This is especially true if measurement-related variation in the data is larger than the
89 variation associated with the process being observed. In remote sensing, temporal radiometric image distortion
90 is common in time-series and thus normalisation is often required before any interpretations of imagery data can
91 be made. Therefore, the general uptake of UAV-based monitoring technology by many environmental scientists
92 needs to be matched by the development of appropriate methodological protocols. The availability of affordable
93 monitoring equipment is still a relatively new phenomenon and thus there are few critical assessments of the
94 utility of these tools for general use in research.

95 Here we documented the ability of commercial multispectral cameras mounted on UAVs to reliably track high-
96 resolution vegetation area cover changes during a three-year, post-fire recovery period in the Cape Floristic
97 Region, South Africa. Using our data as an example, we propose a practical approach to conducting repeatable
98 vegetation cover change detection for non-remote sensing specialists: 1) assessing the temporal radiometric
99 stability of repeated NDVI images, based on trackable, pseudo invariant features (PIFs), 2) applying relative
100 radiometric normalization by matching PIFs between uncorrected and reference images and 3) using
101 thresholding to isolate vegetation pixels within NDVI images and compute high-resolution changes in
102 vegetation cover over time. The effectiveness of our approach was quantified by comparing remotely sensed
103 vegetation cover estimates with detailed ground area cover measurements that were recorded simultaneously to
104 UAV image surveys.

105 **2. Methods:**

106 **2.1 Study site**

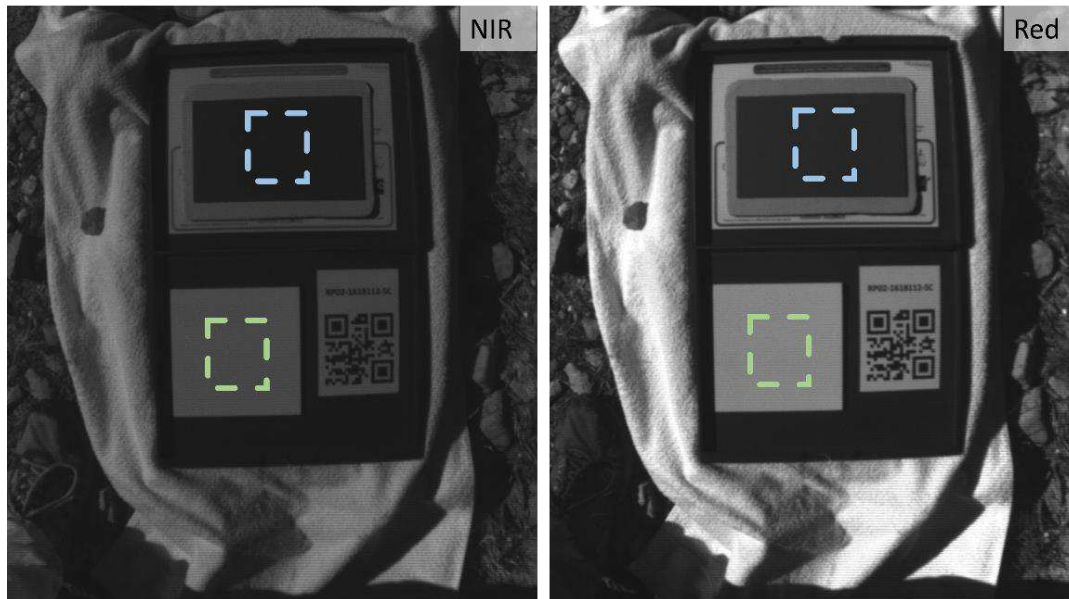
107 We monitored post-fire vegetation recovery over three years at the Drie Kuilen Nature Reserve (33.5805°S,
108 20.0332°E) in the Western Cape of South Africa. The vegetation of this region comprises of the fire-prone,
109 Matjiesfontein Shale Renosterveld and Langeberg Sandstone Fynbos (Mucina & Rutherford, 2006). The
110 region is semi-arid with <300 mm mean annual rainfall. We conducted our study in a Fynbos and a
111 Renosterveld site located within a kilometre of each other (with < 200 m altitude difference), either side of a
112 distinct ecotone. We monitored 12 permanent 16 m² plots within each site (i.e. Fynbos × 12 and Renosterveld ×
113 12) after a controlled burn in May 2016. Controlled burns cleared plots of all above ground biomass (van Blek
114 *et al.*, 2021 a).

115 **2.2. Multispectral imagery collection using UAVs:**

116 Starting in February 2017, aerial imagery of Fynbos and Renosterveld sites was captured twice a year using
117 UAVs (DJI Phantom 3 Professional - <https://www.dji.com>) and a mounted multispectral camera (Parrot sequoia
118 - <https://www.parrot.com>). The Parrot sequoia was mounted onto the DJI Phantom 3 Professional with a Parrot
119 Sequoia Mount Kit. Unfortunately, the camera mount did not include a gyro meaning that the camera position
120 was fixed relative to the UAV. This meant that care had to be taken to keep the camera positioning on the UAV
121 constant over repeated surveys. On each survey date; hundreds of individual images, with >80% overlap, were
122 captured from a height of 15 – 20 m during a 2D grid flight path. Survey flight paths were programmed using
123 AtlasFlight (<https://micasense.com>) software. The Parrot sequoia captured red (640-680nm) and near infrared
124 (NIR) (770-810nm) bands using multispectral sensors and also captured RBG (Red, Green, Blue) images.
125 Repeated UAV surveys were always conducted as close to midday as possible to reduce shadows around
126 vegetation. Flight times did not exceed 25 minutes due to battery-life limitations. UAV surveys were also
127 conducted on days with 0% cloud cover.

128 Single-band red and NIR images were calibrated using standard Pix4D Mapper (<https://www.pix4d.com>)
129 software calibrations. These included i) camera corrections (e.g. vignetting, ISO, dark current etc.), ii)
130 radiometric calibration panel reflectance values and iii) sunshine sensor data. Immediately before and after
131 surveys, images of a MicaSense calibrated reflectance panel (<https://support.micasense.com>) and 18% gray
132 cards were captured (Fig. 1). This allowed for the Pix4D Mapper image-processing software to apply

133 radiometric calibrations to single band images (e.g. red and NIR) via the empirical line method before
134 generating multi-band vegetation indices (e.g. NDVI). The Pix4D software used only a single radiometric target
135 to perform image corrections but the other target served as a backup in case of calibration images being over-
136 exposed. Additionally, a Sunshine Sensor module (<https://www.parrot.com>) recorded incoming solar irradiance
137 and reflected irradiance during surveys to account for changes in solar intensity. The sunshine sensor module
138 was fitted to the Phantom 3 Professional using a Parrot Sequoia Mount Kit.



139

140 **Fig. 1** Radiometric calibration panels including the Micasense calibrated reflectance panel (green squares) and
141 18% gray cards (blue squares).

142

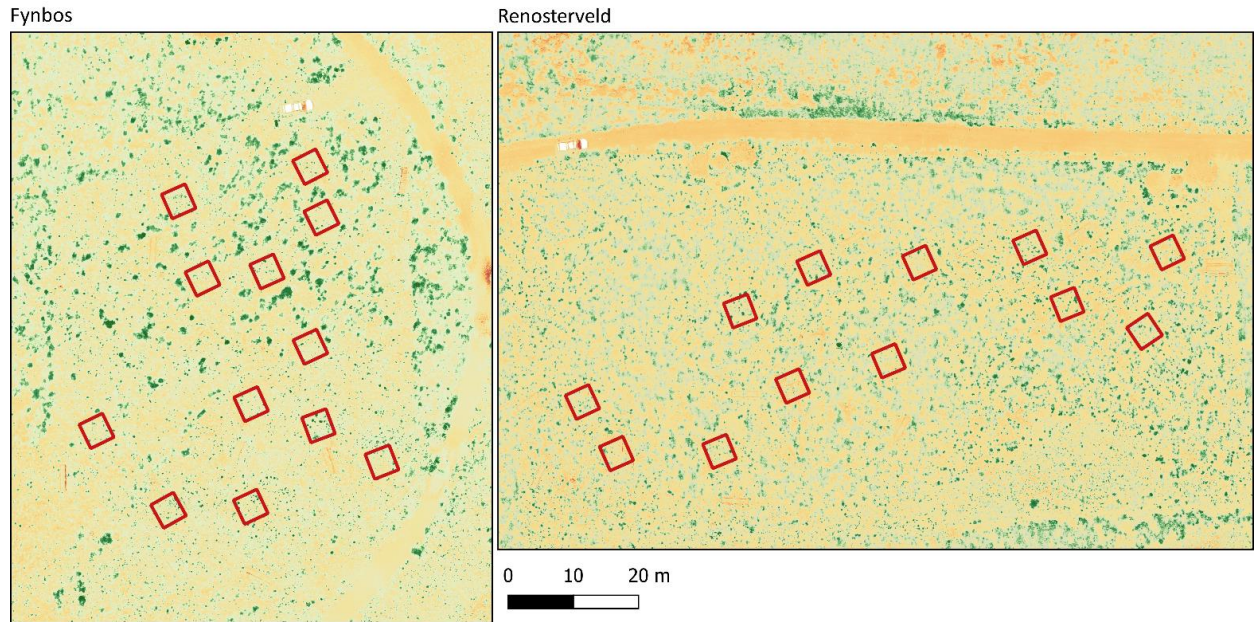
143 For each survey date, corrected and calibrated red and NIR images were orthorectified and converted into
144 composite single-band orthomosaic images which covered the full area of the sites (**Fig. 2**). Red and NIR
145 orthomosaic images were automatically aligned by Pix4D software using the known lens offset positions on the
146 camera. Orthomosaic NDVI images were then generated using the equation:

147 1)
$$NDVI = \frac{NIR-RED}{NIR+RED}$$

148

149 Repeated orthomosaic NDVI layers were produced for Fynbos and Renosterveld sites over 5 separate surveys
150 (i.e. Feb 2017, Oct 2017, Apr 2018, Oct 2018, May 2019) (**Fig. 2**). In addition to NDVI orthomosaic images,
151 matching RGB orthomosaic images were also generated for comparison at each time step.

152



153

154

155

156

157

Fig. 2 NDVI orthomosaic layers for post-fire Fynbos and Renosterveld sites from a single time-step. Colour scales represent NDVI -1 (red): 1 (green). Red squares represent 16 m² focal plots in which ground measurements of vegetation area were taken. Repeated orthomosaic layers were obtained for Nov 2016, Feb 2017, Oct 2017, Apr 2018, Oct 2018, May 2019.

158

159

2.3 Relative radiometric normalization of NDVI orthomosaic images

160

2.3.1 Tracking pseudo-invariant features (PIFs) within NDVI image layers to assess temporal distortion in repeated imagery.

161

162

While we followed the recommended protocols for the collection and calibration of red and NIR images using

163

the Parrot Sequoia and Pix4DMapper, we found that additional steps were required to obtain temporal

164

radiometric stability in repeated orthomosaic NDVI images. We achieved this by applying additional

165

radiometric corrections directly to NDVI orthomosaic images. The radiometric stability of the NDVI pixel

166

values in repeated orthomosaic image layers was investigated by tracking the variation in pseudo-invariant

167

features (PIFs) within the NDVI image layers over time. PIFs are commonly used for the relative radiometric

168

normalization of time-series data which is often required for accurate land cover detection ([Bao et al., 2012](#);

169

[Zhou et al., 2016](#)). Here PIFs were considered to be landscape features or objects within images which were not

170

expected to vary over time in terms of their NDVI value, regardless of factors such as season or time after fire.

171

PIFs were thus intended to reveal variation in the images which was not driven by real landscape changes, but

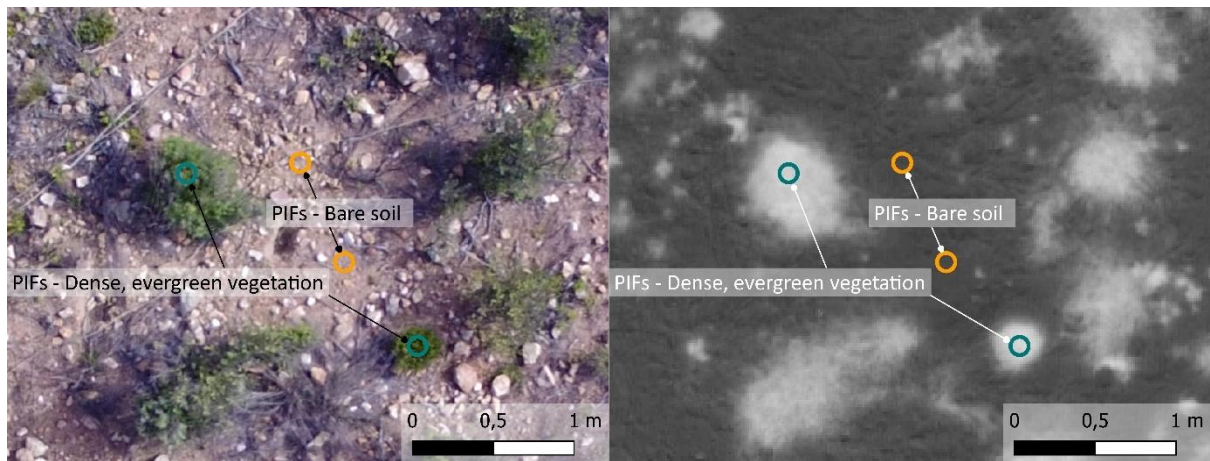
172

rather by artifacts of the imagery acquisition process. PIFs included a trackable low-value NDVI feature and a

173 high-value NDVI feature. PIFs were tracked over time using polygons in fixed positions aligned with the
174 orthoimages. A combination of low and high value PIFs were necessary to monitor image stability over the full
175 spectrum of possible pixel values. This is because temporal radiometric distortion in pixel values over repeated
176 images was not necessarily equal across all pixels and could arise from the compression or expansion of NDVI
177 scale rather than image-wide pixel value shifts. Pixel frequency histograms were used to visually compare
178 image pixel values over time in corrected and uncorrected imagery.

179 2.3.2 Selection of pseudo-invariant features

180 We selected bare soil patches as low-NDVI-value PIFs (**Fig. 3**) because we assumed that soil NDVI values
181 should not change over time and should have consistent, low NDVI value. The central pixels of dense, unburnt,
182 off-plot, evergreen shrubs were selected as high value PIFs (**Fig. 3**). We assumed that these pixels represented
183 100% evergreen leaf coverage with no soil pixels included. Using dense, evergreen vegetation polygons as high
184 PIFs could be problematic in some cases seeing that some seasonal variation in leaf NDVI might be expected.
185 Ideally, PIFs should be inert, whereas vegetation NDVI values may vary. However, in this scenario, we argue
186 that the central pixels of dense, evergreen, deep-rooted shrubs were likely to have minimal seasonal
187 photosynthetic variation ([van Blerk et al., 2021 b](#)) and were thus the best available option for a high value PIF.
188 For each PIF, multiple polygons (>20) were chosen and tracked over time.



189

190 **Fig. 3** Example of pseudo-invariant features (PIFs) shown in RGB (left) and greyscale NDVI (right) images.
191 Low NDVI value PIFs = bare soil (orange circles). High-value PIFs = dense, evergreen vegetation (blue circles).

192

193

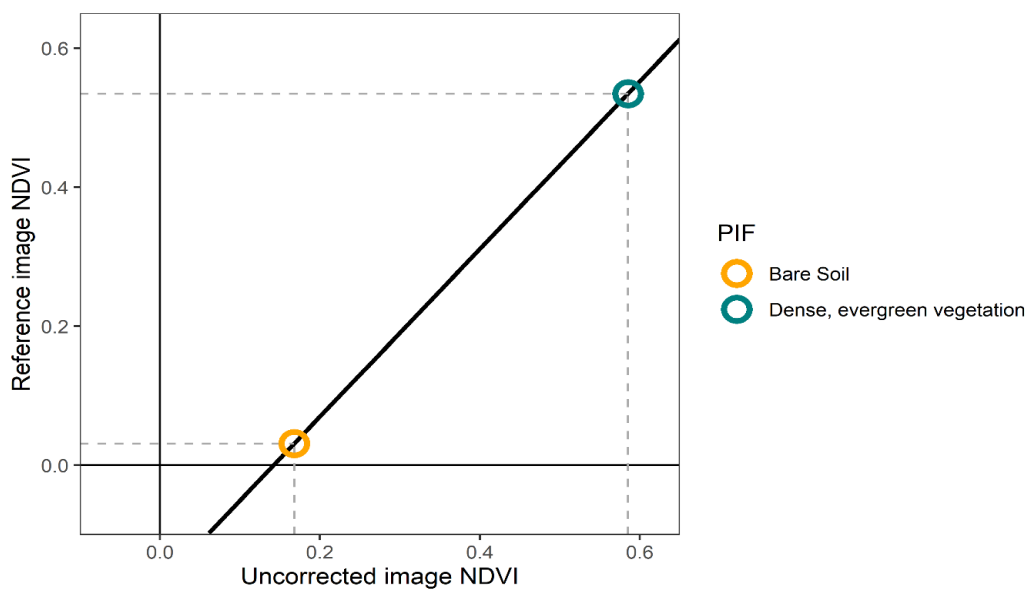
194 2.3.3 Image normalization procedure

195 Relative radiometric normalization of imagery was used to adjust the pixel values of image layers relative to the
196 PIFs of the first image in the sequence (i.e. reference image). Pixel adjustment equations were modeled on the
197 linear relationship between the PIF values of uncorrected and reference images (Fig. 4), using the sum of least
198 squares. Pixel values of uncorrected images were modified to their target values according to the formula

199 2)
$$y_i = mx + c$$

200 Where y = the value of a given pixel i within the reference image, m = slope of the relationship between
201 uncorrected PIFs and reference PIFs, c = intercept of the relationship between uncorrected PIFs and reference
202 PIFs.

203



204

205 **Fig. 4** Diagram showing the relationship between PIFs from an uncorrected image and reference image (i.e. first
206 image in time-series). Dashed grey lines trace the PIF values to their positions on the x and y axes. Trendline is
207 displayed in black and represents the line from which the normalization equation is derived. This process was
208 applied to images from each survey date.

209

210

211

212

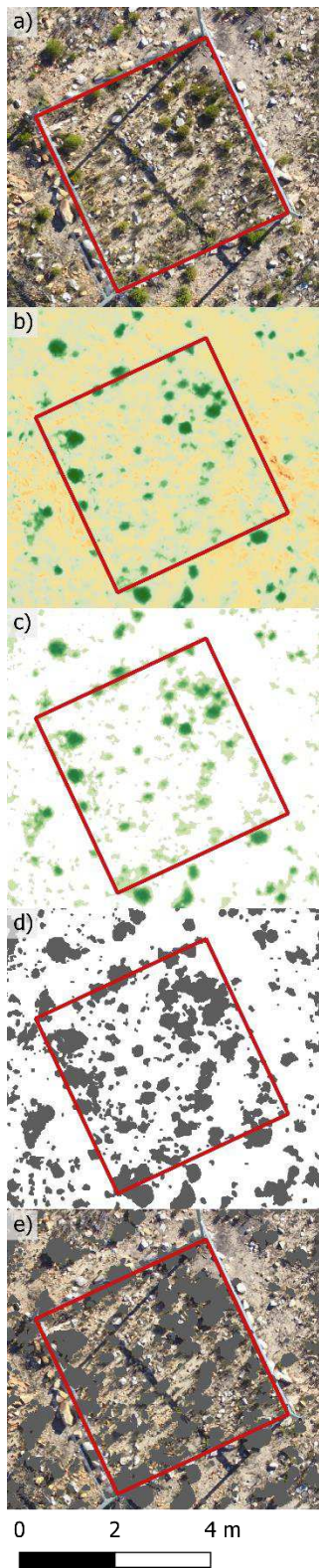
213 **2.4. Extracting data from imagery**

214 We used a combination of QGIS (QGIS Development Team, 2009. QGIS Geographic Information System.
215 Open Source Geospatial Foundation. <http://qgis.org>) and R (R Core Team 2020. <https://www.r-project.org>) to
216 extract and summarize pixel values from the multispectral imagery over the 5 survey dates. For both the Fynbos
217 and Renosterveld site, polygons were used to delineate the 16 m² treatment plots in the series of aligned RGB
218 (Fig. 5 a) and NDVI (Fig. 5 b) orthomosaic layers over time. RGB image layers were used as a guide for
219 choosing the correct positioning of polygons. The bases of the upright steel poles in the corner of each plot
220 served as points of orientation for alignment.

221 The `exact_extract()` function was used to summarize NDVI pixel values from within plot polygons or fixed PIF
222 polygons.

223 **2.5. Calculating vegetation area cover using NDVI-thresholding**

224 We used a simple NDVI image thresholding technique to isolate vegetation pixels from the soil pixels within the
225 NDVI orthomosaic images (Fig. 5 c). This entailed removing all pixels from NDVI orthomosaic layers below a
226 chosen NDVI threshold value < 0.2 (Fig. 5 c). The presence/absence of pixels then corresponded with
227 vegetation cover versus no vegetation cover in images respectively, allowing for the quantification of high-
228 resolution area cover per plot (Fig. 5 d). The chosen NDVI threshold value was higher than the mean values of
229 soil PIFs and was visually adjusted in QGIS until it most successfully corresponded to vegetation patches. Area
230 cover was measured by multiplying the number of pixels above the threshold of 0.2 NDVI by the squared pixel
231 area. Overlaying the threshold images onto RGB images allowed for a visual comparison of threshold area and
232 visible vegetation patches (Fig. 5 e). Because NDVI pixel density histograms were unimodal, we did not
233 attempt to use automatic thresholding algorithms (e.g. Otsu, 1979). Instead, we chose to manually select and
234 adjust thresholds based on available pixel information. We also considered automatic edge detection methods
235 (e.g. level setting) to calculate the area of vegetation within NDVI images (e.g. Ghazal et al., 2015) but due to
236 the computational complexities of such a method, we settled with our simpler, more accessible approach.



237

238 **Fig. 5** Process of extracting NDVI-derived area cover data from images. **a)** RGB orthomosaic showing
 239 vegetation and soil. Red squares represent 16m² focal plots. **b)** NDVI orthomosaic -1 (red): 1 (green) **c)**
 240 Vegetation-specific NDVI using a threshold of NDVI > 0.2 **d)** Area cover polygons derived from vegetation
 241 specific NDVI **e)** Overlay of vegetation area-cover polygons on RGB images for visual comparison.

242

243 **2.6. Ground-truthing data**

244 Detailed plant demographic surveys were conducted at the same time as UAV-based surveys. Demographic
245 surveys included counting and measuring the area and height of every plant within each of the 12, 16 m² focal
246 plots. Over 60 000 individual measurements were made over the duration of the experiment ([van Blerk *et al.*,
247 2021 a](#)).

248 Linear relationships between UAV-based area measurements and ground area measurements were compared
249 between uncorrected and corrected imagery. R-squared values were calculated using the sum of least squares.

250

251

252

253

254

255

256

257

258

259

260

261

262

263

264

265

266 **3. Results:**

267 *3.1 Assessing temporal image distortion in uncorrected NDVI time-series imagery using pseudo invariant*
268 *features*

269 Bare soil PIF polygons clearly showed elevated NDVI values in Fynbos during October 2018 (**Fig. 6 c**) and
270 corresponded with a large increase in mean plot NDVI (**Fig. 6 a**). Soil pixel values had a strong overall
271 influence on mean plot NDVI because the majority of image pixels represented soil in the post-fire environment.
272 Renosterveld soil PIF polygons also displayed slightly reduced NDVI values in April 2018 and May 2019 (**Fig.**
273 **6 d**), contributing to lower mean plot NDVI values during those months (**Fig. 6 b**). In both Fynbos and
274 Renosterveld, shifts in soil PIF polygons did not correspond with equivalent shifts in dense, evergreen
275 vegetation polygons (**Fig. 6 e, f**). This indicated that the nature of the image radiometric distortion was non-
276 linear and was not an equal shift in pixel values across the full range of NDVI values. Higher NDVI values were
277 relatively unaffected by contrast problems which so clearly affected low NDVI values.

278 Image pixel density histograms (**Fig. 7**) provided a visual confirmation that compression or expansion of
279 histogram peaks had occurred in some layers (e.g. October 2018 Fynbos) rather than range shifts which would
280 have shown equal shifts in all pixels.

281

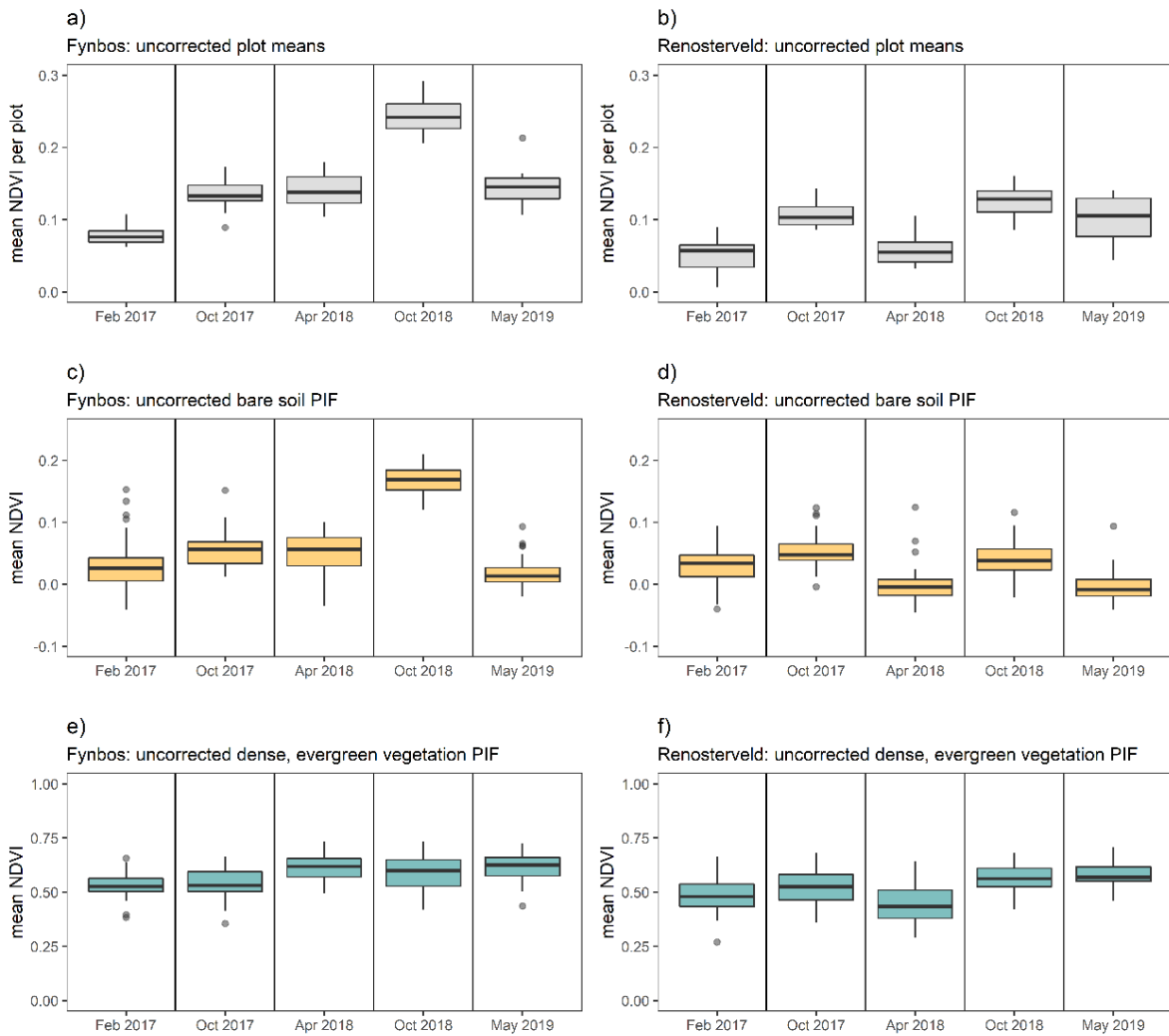
282

283

284

285

286



287

288 **Fig. 6 a, b** Mean NDVI per plot using uncorrected Fynbos and Renosterveld orthomosaic NDVI images. **c, d**
 289 mean NDVI of bare soil PIFs (pseudo invariant feature) and **e, f** mean NDVI of dense, evergreen vegetation
 290 PIFs for uncorrected image layers.

291

292 **3.2 Identifying possible software and hardware issues**

293 Image radiometric distortion over time, represented by non-matching histogram peaks (**Fig. 7**), was not
 294 introduced by any of the Pix4D image processing corrections applied during the production of the NDVI
 295 orthomosaic images. This was tested by re-processing imagery using different combinations of software
 296 corrections available. These corrections included i) camera corrections (e.g. vignetting, ISO, dark current etc.),
 297 ii) radiometric calibration panel corrections, iii) sunshine sensor corrections. Camera corrections dramatically
 298 improved the similarity of histograms (shape and range) over time relative to the raw orthomosaic images.

299 Correcting red and near-infrared (NIR) image layers using different radiometric calibration panels (i.e. light

300 panel versus 18% grey panel) in Pix4D had little effect on the output data suggesting that the panels were
301 reliable reflectance references. Additionally, applying image corrections using radiometric calibration panels
302 and/or the sunshine sensor resulted in equivalent output image pixel density histograms, indicating redundancy
303 between radiometric calibration using field panels and the sunshine sensor, as suggested by the developer.
304 Overall, these tests indicated that image distortion in some layers was not directly a result of software
305 processing through Pix4D or calibration panel issues. Rather, this finding points to deeper issues associated with
306 the functioning of the camera or survey conditions during some UAV flights including camera angle, camera
307 temperature, convective warm air, atmospheric moisture and sun angle.

308 Notably, we observed that the UAV would briefly tilt when taking photographs during some surveys. This could
309 potentially lead to significant changes in the angle of the camera relative to the ground. If this was the cause of
310 image distortion in some layers, then the clear contrast between the distortion effects on pixels with low NDVI
311 values (i.e. soil PIFs) versus those with high values (i.e. dense, evergreen vegetation PIFs) could be explained
312 by differences in the sensitivity of object reflectivity to slight differences in camera/sun angle during the
313 surveys. For example, the complex, diffuse reflectance of fine-leaved vegetation is not likely to vary strongly
314 with variation in measurement angles, suggesting that slight changes in sun or camera angle had relatively little
315 effect on the reflectance values captured by the camera. Conversely, angular or flat surfaces, such as soil and
316 rock, could be more susceptible to such angle-related factors. Additionally, other complex, angle-related
317 phenomena, such as the bidirectional reflectance effect, could differentially alter the reflectance characteristics
318 of red and NIR wavelengths based on sun and sensor angles thus leading to complex image distortion (Hapke,
319 1981). While we endeavoured to uncover the exact cause of image distortion, the cryptic nature of this distortion
320 proved to be too complex to identify with the information available. Therefore, we felt that post-processing
321 image correction (i.e. direct correction on NDVI layers) would be the most robust and practical solution.

322 *3.3 Image normalisation based on PIFs*

323 Relative radiometric normalisation resulted in matching PIFs over repeated images in both sites (Fig. 7). This
324 had the effect of closely aligning the peaks of pixel frequency histograms over time (Fig. 7). Uncorrected image
325 histograms were relatively similar to corrected image histograms at most time-periods in both sites with the
326 exception of the Fynbos site in October 2018 where a large transformation effect is clearly visible (Fig. 7). It
327 was apparent that matching dense, evergreen vegetation PIFs had a relatively small effect on the shape of
328 histograms compared to the effect of matching bare soil PIFs, which strongly shifted histogram peaks.

329 Importantly, even after matching dense, evergreen vegetation PIFs over time, the density of the histograms
330 toward upper NDVI values was still able to increase over time, indicating an increase in the fraction of
331 vegetation relative to bare soil. In corrected imagery, plot NDVI patterns (**Fig. 7**) did not include the large,
332 spurious increases in mean plot NDVI which were previously related to noise in the bare soil PIFs in
333 uncorrected imagery (**Fig. 6**).

334

335

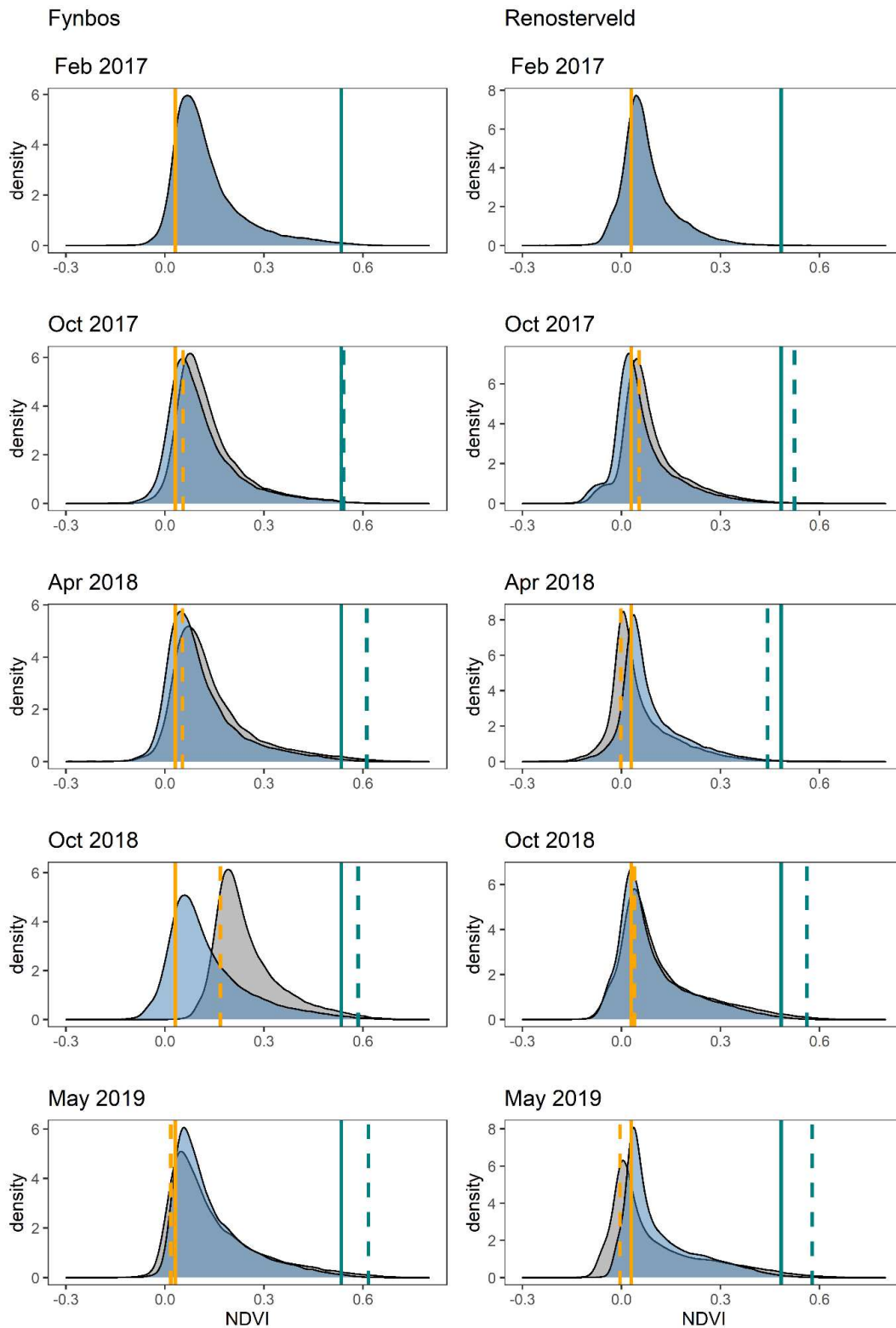
336

337

338

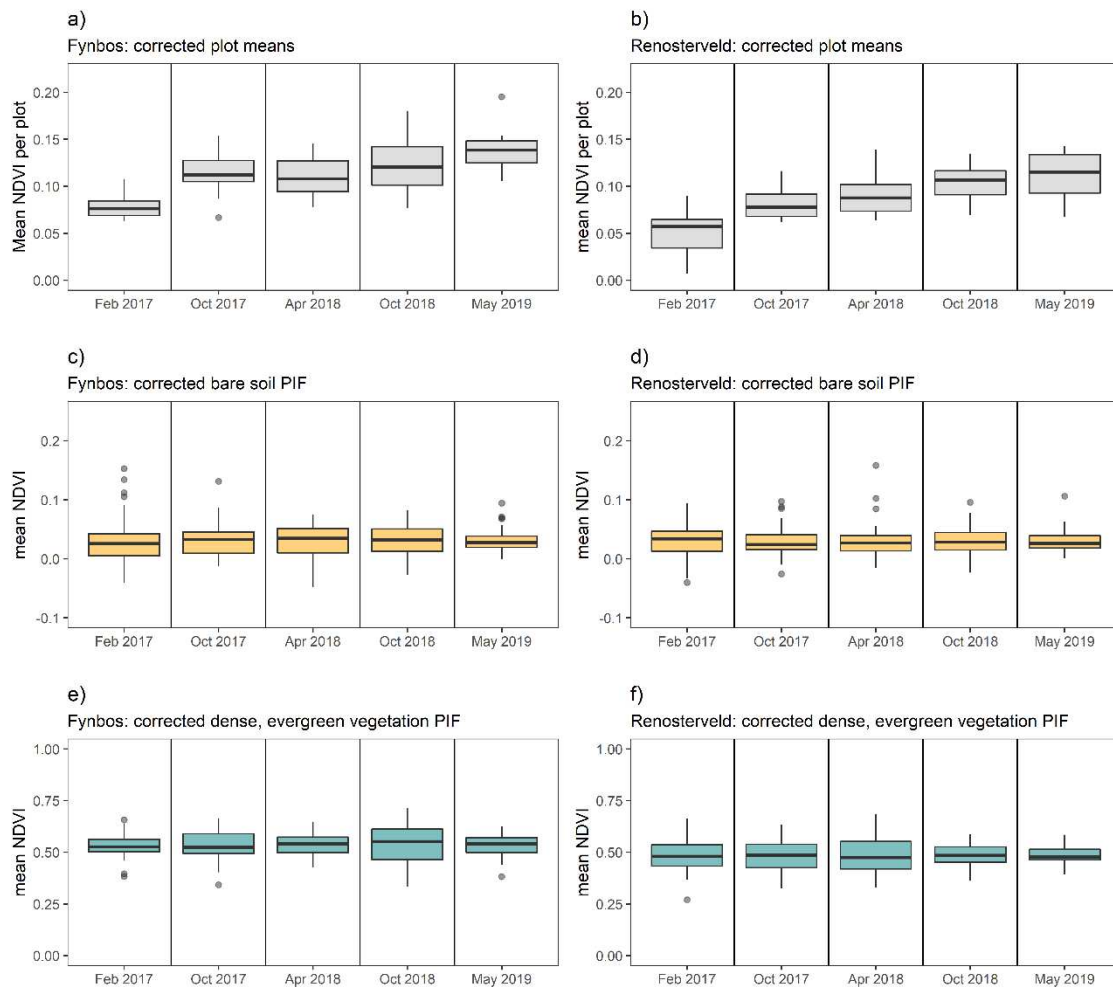
339

340



341

342 **Fig. 7** NDVI pixel density histograms for uncorrected (grey) and corrected (blue) image layers. Solid vertical
 343 lines represent corrected PIF values for bare soil (yellow) and dense, evergreen vegetation (blue). Dashed
 344 vertical lines represent uncorrected PIF values.



345

346 **Fig. 8 a, b** Mean NDVI per 16 m² plot using corrected Fynbos and Renosterveld orthomosaic NDVI images. **c,**
 347 **d**) mean NDVI of bare soil PIFs (pseudo invariant feature) and **e, f**) mean NDVI of dense, evergreen vegetation
 348 PIFs for corrected image layers.

349

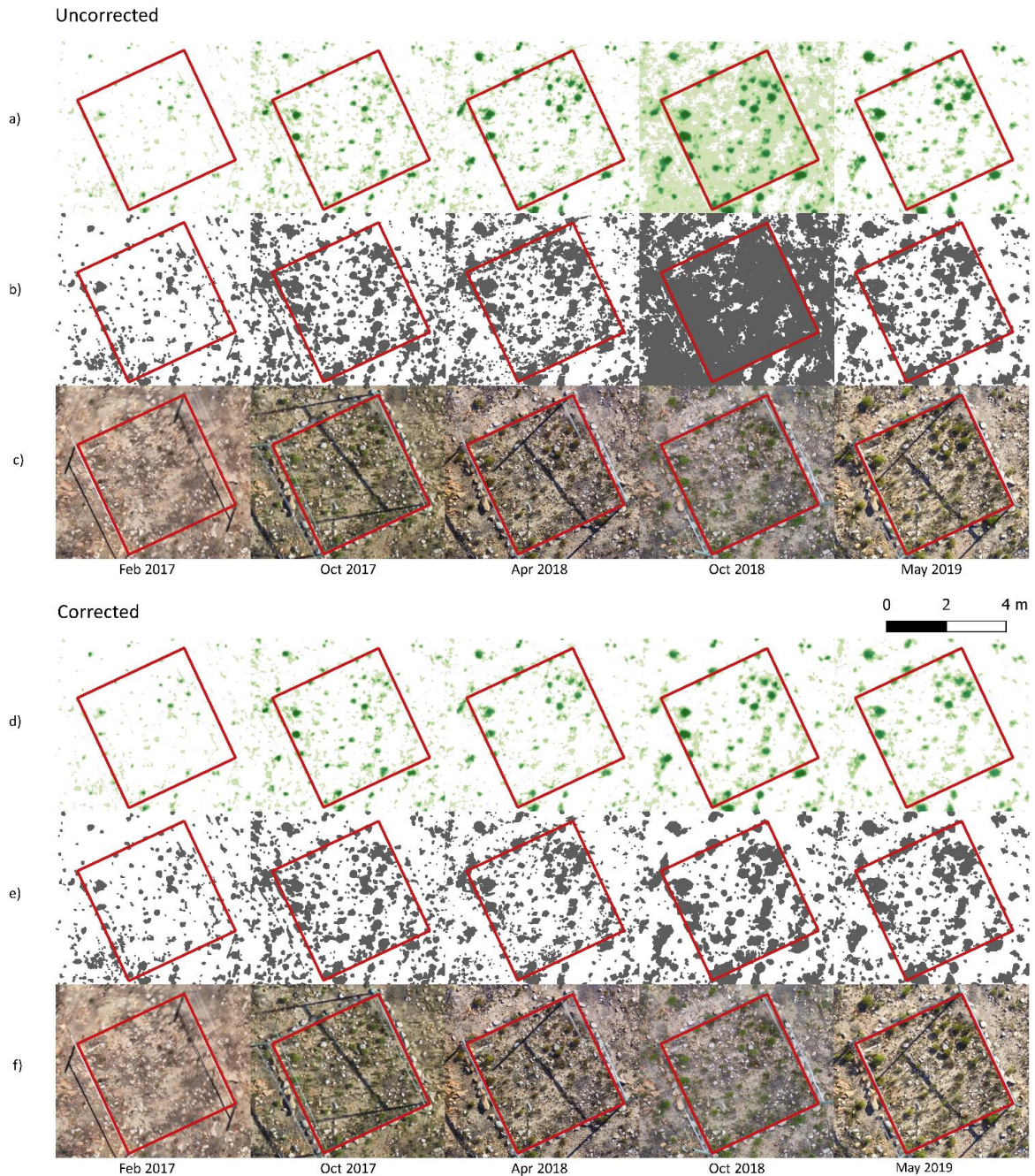
350 3.4 Using NDVI thresholding to measure vegetation cover

351 A threshold of NDVI < 0.2 was found to accurately isolate vegetation patches from the environmental features
 352 (i.e. rock and soil) (**Fig. 9**). This was confirmed visually using the RGB images. However, consistently
 353 isolating vegetation using a common threshold was problematic using uncorrected imagery if pixel distortion
 354 issues were present in some layers, such as in the uncorrected Fynbos layers in October 2018). Image distortion
 355 led to soil values being included above the chosen NDVI threshold (**Fig. 9**).

356 In the case of the Fynbos Oct2018 layer, this was explained by the compression of low values toward high
 357 values which was clearly visible in the frequency histogram (**Fig. 7, 8**). Inclusion of soil pixels above the
 358 vegetation threshold had obvious negative implications for area estimates and vegetation specific signal

359 estimates.

360 Our method of image normalisation solved this problem and allowed for a common NDVI threshold to reliably
361 isolate vegetation patches over all time steps (**Fig. 9**). The ability of image correction to solve the thresholding
362 problem provided added confidence that our chosen image normalisation procedure was appropriate.



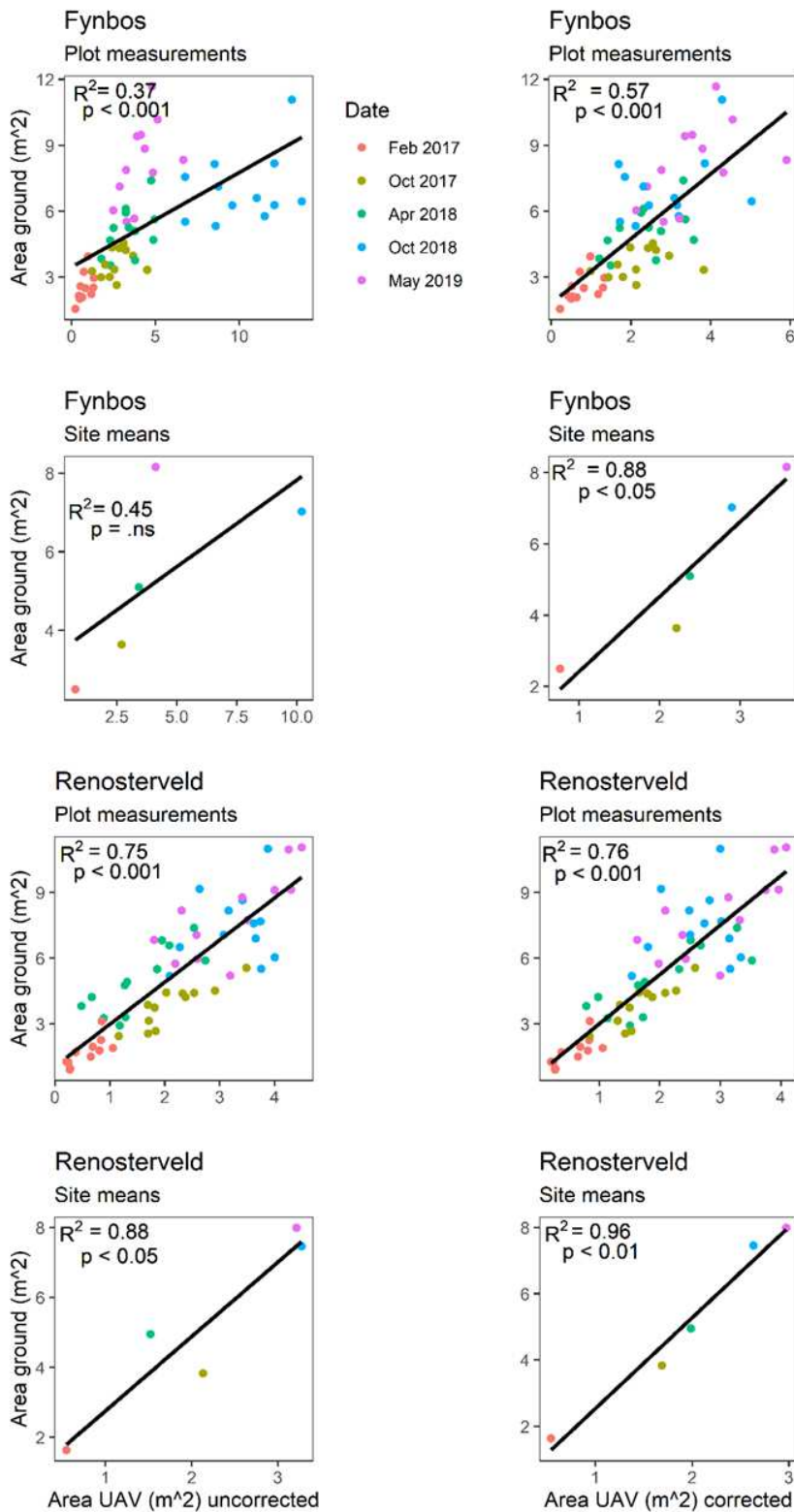
363

364 **Fig. 9 a, d)** Post-fire vegetation-specific NDVI ($NDVI > 0.2$) changes within a 16 m^2 focal plot over time.
365 White areas represent NA values while colour pixels represent NDVI values of vegetation. **b, e)** Vegetation
366 area cover polygons. **c, f)** RGB images for comparison with vegetation area cover polygons.

367

368 **3.5 Ground truthing UAV data**

369 Relative radiometric normalisation of imagery significantly improved the correlations between UAV-based
370 vegetation cover measurements and corresponding ground-based measurements (Fig. 10) within 16 m² focal
371 plots. The effect of normalisation was most evident at the Fynbos site where the uncorrected images had a high
372 degree of temporal inconsistency (e.g. October 2018 orthomosaic). At the plot-level, there was substantial
373 variation between UAV-based and ground-based vegetation cover measurements. However, this was likely to be
374 the result of variation within ground-based measurements instead of inconsistencies in UAV-based
375 measurements. Ground-based area measurements did not account for complex canopy shapes of plants and
376 overlap within plots. When summarised at the site level, relative radiometric normalisation dramatically
377 improved correlations between UAV and ground-based area measurements and resulted in strong relationships
378 (i.e. $R^2 > 0.87$). This was particularly relevant in the Fynbos site where UAV-based and ground-based area
379 measurements were not significantly correlated when using uncorrected imagery.



380

381 **Fig. 10** Comparison of vegetation area cover (m^2) per $16 m^2$ focal plot, obtained from ground-based
 382 measurements ('Area ground') and UAV-based measurements ('Area UAV'). UAV-based vegetation cover
 383 measurements made using uncorrected (left column) and corrected (right column) images are displayed side-by-
 384 side. Plot measurements include the measured vegetation area cover of each focal plot. Site means represent the
 385 mean of plot area cover measurements for each date.

386

387 4. Discussion

388 Our study demonstrated that UAV-mounted multispectral cameras can be a powerful addition to the ecologists'
389 toolbox as it enables repeatable monitoring of high-resolution (i.e. sub-meter) vegetation cover changes over
390 larger spatial scales. However, we caution against adopting a “black-box” approach when using UAV and image
391 processing technology which can result in spurious patterns in data. Our protocol used pseudoinvariant features
392 (PIFs) to assess the radiometric consistency in repeated NDVI images after software calibrations. We then
393 applied appropriate normalisations to images based on PIFs and utilised a simple thresholding method for rapid
394 measurement of vegetation area cover. Extensive ground-truthing revealed that our procedure improved the
395 accuracy of UAV-based vegetation cover measurements.

396 Default software calibrations in Pix4D (i.e. camera corrections, sunshine sensor and radiometric calibration
397 panels) fell short of producing radiometrically stable NDVI pixel values over time for analysis. This was not
398 necessarily a fault of the software but was rather related to a tendency for uncontrolled environmental, sensor or
399 user error to easily be introduced into repeated surveys (Teillet 1986; Hall *et al.*, 1991). The key challenges to
400 overcome included the identification and correction of image radiometric distortion over the full time-series
401 sequence. Image radiometric distortion can introduce spurious patterns into time-series data, thus limiting the
402 ability to correctly describe vegetation patterns over time (Teillet, 1986; Hall *et al.*, 1991; Zhou *et al.*, 2016).
403 This was clear in the Fynbos image-layers where values representing natural seasonal changes in vegetation
404 were strongly skewed by a single distorted image in October 2018. The effect of image-distortion could also be
405 more subtle and lead to exaggerated vegetation patterns in the data (e.g. Renosterveld April 2018 and May
406 2019).

407 We showed that simple relative radiometric image normalisation approaches can be carried out directly on
408 NDVI orthomosaic layers and can be successful using a minimum of two pseudo-invariant features in the
409 landscape, as long as their values cover a wide enough range of pixel values on the response variable scale (e.g.
410 low and high NDVI). Through the identification of PIFs, the presence and nature of image distortion is revealed,
411 allowing for an appropriate correction to be applied to images. Unavoidably, applying relative radiometric
412 normalization to image pixel values based on dense, evergreen vegetation PIFs in reference images may reduce
413 some of the natural temporal variation in upper NDVI values, associated with leaf-level NDVI seasonality.
414 However, seeing that there was no alternate method to assess the quality of upper NDVI pixel values, we felt
415 that applying an equal normalization across all images was the fairest treatment of the data. Furthermore,

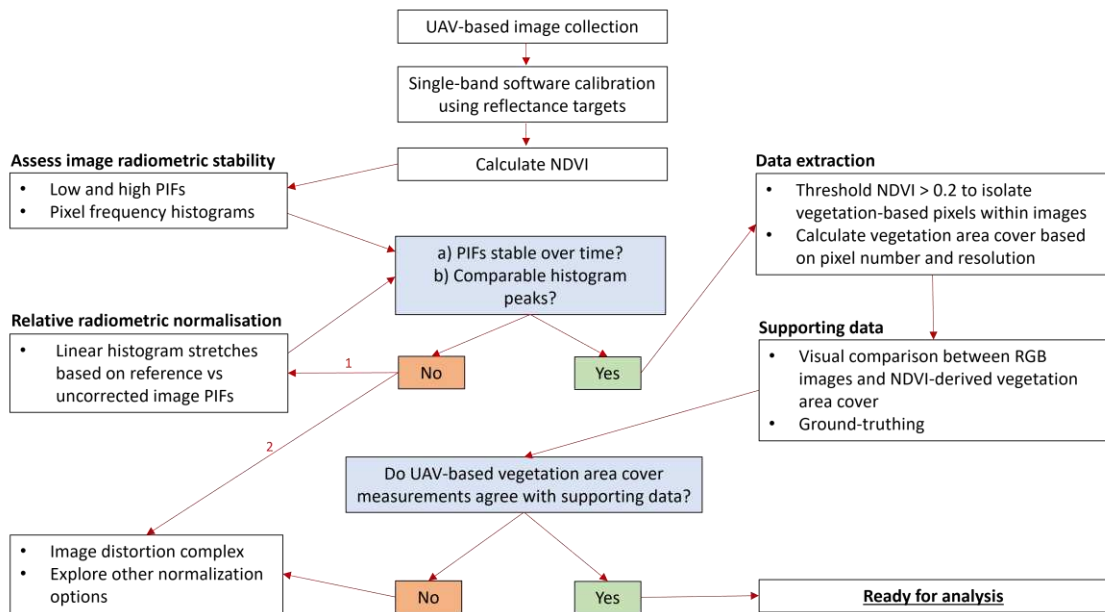
416 normalization of upper pixel values by matching PIFs to the first image of the time-series did not hinder changes
417 in the shape of density histograms over time. For example, increases in histogram density toward higher NDVI
418 values was apparent over time in corrected imagery and represented increases in vegetation cover.

419 Normalization of upper NDVI pixel values was intended to reduce the chance of Type 1 errors occurring (i.e.
420 detecting vegetation changes that do not exist) (Dekking *et al.*, 2005). While the bias towards avoiding Type 1
421 errors has been identified amongst scientists (Anderegg *et al.*, 2014), we purposefully avoided Type 1 errors
422 because it was apparent how easily they could be introduced into data even by slight image distortion. Notably,
423 image normalization based on features within images was superior to normalization based on histograms
424 themselves. Histogram matching was not appropriate because it results in near-identical histograms over time,
425 thus muting any vegetation change signals within images.

426 While we show that natural landscape features can be used successfully to conduct relative radiometric
427 normalization, this possibility is strongly dependent on the features of the specific environment being surveyed
428 (e.g. evergreen shrubs, stable soils). If no stable soil value or vegetation value exists in the landscape, our
429 proposed methodology would not be applicable. Therefore, including permanent ground control points would
430 ideally replace the organic (bare soil and dense, evergreen vegetation) PIFs used in our methodology. We also
431 recommend including RGB imagery in UAV-based surveys. The ability to visually verify that vegetation indices
432 and area cover polygons correspond with the actual patterns of vegetation cover on the ground is invaluable.

433 **Recommendations**

434 We recommend adopting a protocol to identify and correct temporal radiometric noise in repeated imagery data
435 before extracting ecological or environmental information from imagery (Fig. 11). This should be carried out
436 even if imagery processing software includes calibration and normalisation procedures. Additionally, we
437 recommend testing the quality of UAV-based data by including some degree of ground-truthing. Together, these
438 steps can ensure the production of reliable time-series data.



439

440 **Fig. 11** Protocol for UAV-based vegetation cover change monitoring.

441 Overall, if used with caution, UAV-mounted multispectral cameras greatly improve the potential for monitoring
 442 fine-scale vegetation changes (sub-meter resolution) across intermediate spatial and temporal scales. This could
 443 lead to a better understanding of how vegetation processes relate to patterns observed at larger spatial scales.

444

445

446

447

448

449

450

451

452

453

454 **References:**

- 455 Anderegg, W. R., Callaway, E. S., Boykoff, M. T., Yohe, G., & Root, T. Y. L. (2014). Awareness of both type 1
456 and 2 errors in climate science and assessment. *Bulletin of the American Meteorological Society*, 95(9),
457 1445-1451.
- 458 Aplin, P. (2005). Remote sensing: ecology. *Progress in Physical Geography*, 29(1), 104-113.
- 459 Bao, N., Lechner, A. M., Fletcher, A., Mulligan, D., Mellor, A., & Bai, Z. (2012). Comparison of relative
460 radiometric normalization methods using pseudo-invariant features for change detection studies in rural
461 and urban landscapes. *Journal of Applied Remote Sensing*, 6(1), 063578.
- 462 Bergstedt, J., Westerberg, L., & Milberg, P. (2009). In the eye of the beholder: bias and stochastic variation in
463 cover estimates. *Plant ecology*, 204(2), 271-283.
- 464 Cammeraat, E., van Beek, R., & Kooijman, A. (2005). Vegetation succession and its consequences for slope
465 stability in SE Spain. *Plant and Soil*, 278(1), 135-147.
- 466 Cramer, M. D., & Hoffman, M. T. (2015). The consequences of precipitation seasonality for Mediterranean-
467 ecosystem vegetation of South Africa. *PloS one*, 10(12), e0144512.
- 468 Dekking, F. M., Kraaikamp, C., Lopuhaä, H. P., & Meester, L. E. (2005). *A Modern Introduction to Probability*
469 *and Statistics: Understanding why and how*. Springer Science & Business Media.
- 470 Duveiller, G., & Defourny, P. (2010). A conceptual framework to define the spatial resolution requirements for
471 agricultural monitoring using remote sensing. *Remote Sensing of Environment*, 114(11), 2637-2650.
- 472 Esler KJ, Von Staden L, Midgley GF. 2015. Determinants of the Fynbos/ Succulent Karoo biome boundary:
473 insights from a reciprocal transplant experiment. *South African Journal of Botany* 101: 120–128.
- 474 Estrany, J., Ruiz, M., Calsamiglia, A., Carriquí, M., García-Comendador, J., Nadal, M., ... & Gago, J. (2019).
475 Sediment connectivity linked to vegetation using UAVs: High-resolution imagery for ecosystem
476 management. *Science of the Total Environment*, 671, 1192-1205.
- 477 Ghazal, M., Al Khalil, Y., & Hajjdiab, H. (2015, December). UAV-based remote sensing for vegetation cover
478 estimation using NDVI imagery and level sets method. In *2015 IEEE International Symposium on Signal*
479 *Processing and Information Technology (ISSPIT)* (pp. 332-337). IEEE.

480 Gitas, I., Mitri, G., Veraverbeke, S., & Polychronaki, A. (2012). Advances in remote sensing of post-fire
481 vegetation recovery monitoring—a review. *Remote sensing of biomass-Principles and applications, 1*,
482 334.

483 Hall, F. G., Strebel, D. E., Nickeson, J. E., & Goetz, S. J. (1991). Radiometric rectification: toward a common
484 radiometric response among multirate, multisensor images. *Remote sensing of environment, 35*(1), 11-
485 27.

486 Hapke, B. (1981). Bidirectional reflectance spectroscopy: 1. Theory. *Journal of Geophysical Research: Solid*
487 *Earth, 86*(B4), 3039-3054.

488 Marcial-Pablo, M. D. J., Gonzalez-Sanchez, A., Jimenez-Jimenez, S. I., Ontiveros-Capurata, R. E., & Ojeda-
489 Bustamante, W. (2019). Estimation of vegetation fraction using RGB and multispectral images from
490 UAV. *International journal of remote sensing, 40*(2), 420-438.

491 Mucina, L., & Rutherford, M. C. (2006). *The vegetation of South Africa, Lesotho and Swaziland*. South African
492 National Biodiversity Institute.

493 Otsu, N. (1979). A threshold selection method from gray-level histograms. *IEEE transactions on systems, man,*
494 *and cybernetics, 9*(1), 62-66.

495 Port, U., Brovkin, V., & Claussen, M. (2012). The influence of vegetation dynamics on anthropogenic climate
496 change. *Earth System Dynamics, 3*(2), 233-243.

497 Rasmussen, J., Ntakos, G., Nielsen, J., Svensgaard, J., Poulsen, R. N., & Christensen, S. (2016). Are vegetation
498 indices derived from consumer-grade cameras mounted on UAVs sufficiently reliable for assessing
499 experimental plots?. *European Journal of Agronomy, 74*, 75-92.

500 Shoshany, M., Lavee, H., & Kutiel, P. (1995). Seasonal vegetation cover changes as indicators of soil types
501 along a climatological gradient: a mutual study of environmental patterns and controls using remote
502 sensing. *International Journal of Remote Sensing, 16*(12), 2137-2151.

503 Sotille, M. E., Bremer, U. F., Vieira, G., Velho, L. F., Petsch, C., & Simões, J. C. (2020). Evaluation of UAV
504 and satellite-derived NDVI to map maritime Antarctic vegetation. *Applied Geography, 125*, 102322.

505 Slingsby, J. A., Moncrieff, G. R., & Wilson, A. M. (2020). Near-real time forecasting and change detection for

506 an open ecosystem with complex natural dynamics. *ISPRS Journal of Photogrammetry and Remote*
507 *Sensing*, 166, 15-25.

508 Teillet, P. M. (1986). Image correction for radiometric effects in remote sensing. *International Journal of*
509 *Remote Sensing*, 7(12), 1637-1651.

510 Tucker, C. J. (1979). Red and photographic infrared linear combinations for monitoring vegetation. *Remote*
511 *sensing of Environment*, 8(2), 127-150.

512 van Blerk, J. J., West, A. G., Altwegg, R., & Hoffman, M. T. (2021) a. Does a trade-off between growth
513 plasticity and resource conservatism mediate post-fire shrubland responses to rainfall seasonality?. *New*
514 *Phytologist*, 230(4), 1407-1420.

515 van Blerk, J. J., West, A. G., Altwegg, R., & Hoffman, M. T. (2021) b. Post-fire summer rainfall differentially
516 affects reseeders and resprouter population recovery in fire-prone shrublands of South Africa. *Science of*
517 *The Total Environment*, 788, 147699.

518 van Iersel, W., Straatsma, M., Addink, E., & Middelkoop, H. (2018). Monitoring height and greenness of non-
519 woody floodplain vegetation with UAV time series. *ISPRS journal of photogrammetry and remote*
520 *sensing*, 141, 112-123.

521 Veraverbeke, S., Gitas, I., Katagis, T., Polychronaki, A., Somers, B., & Goossens, R. (2012). Assessing post-fire
522 vegetation recovery using red–near infrared vegetation indices: Accounting for background and
523 vegetation variability. *ISPRS Journal of Photogrammetry and Remote Sensing*, 68, 28-39.

524 West, A. G., Dawson, T. E., February, E. C., Midgley, G. F., Bond, W. J., & Aston, T. L. (2012). Diverse
525 functional responses to drought in a Mediterranean-type shrubland in South Africa. *New*
526 *Phytologist*, 195(2), 396-407.

527 Zhang, C., & Kovacs, J. M. (2012). The application of small unmanned aerial systems for precision agriculture:
528 a review. *Precision agriculture*, 13(6), 693-712.

529 Zhou, H., Liu, S., He, J., Wen, Q., Song, L., & Ma, Y. (2016). A new model for the automatic relative
530 radiometric normalization of multiple images with pseudo-invariant features. *International Journal of*
531 *Remote Sensing*, 37(19), 4554-4573.

532 Websites cited:

533 <https://www.dji.com>

534 <https://www.parrot.com>

535 <https://micasense.com>

536 <http://qgis.org>

537 <https://www.r-project.org>

538

539 **Acknowledgements**

540 Funding was generously provided by the NRF (93380 to AGW and 119125 to RA) and ACCESS groups
541 (114696). Thank you to the Plant Conservation Unit for their contribution to the establishment of the Drie
542 Kuilen rainfall manipulation experiment. JJvB was supported by a UCT Science Faculty Scholarship. We are
543 grateful to the NCC and the Drie Kuilen Nature Reserve for providing access and support. Thank you to the
544 many field assistants who were eager to help throughout the research process.

545 **Author contributions**

546 JJvB, AGW, MTH, RA and JS conceptualized the research. JJvB, MTH and AGW collected the data. JJvB
547 processed the data and wrote the manuscript, with contributions from AGW, MTH, RA and JS.

548 **Data availability**

549 The data used during the current study are available from the corresponding author on reasonable request.

550 **Author declarations**

551 The authors have no relevant financial or non-financial interests to disclose.

552